JID: PROCI

Available online at www.sciencedirect.com



ScienceDirect

Proceedings of the Combustion Institute

[mNS;December 5, 2022;12:59]

Proceedings of the Combustion Institute 000 (2022) 1-10

www.elsevier.com/locate/proci

Pressure gradient tailoring effects on vorticity dynamics in the near-wake of bluff-body premixed flames

Samuel H.R. Whitman a, Tyler J. Souders a, Michael A. Meehan a, James G. Brasseur^b, Peter E. Hamlington^{a,*}

^a Paul M. Rady Department of Mechanical Engineering, University of Colorado, Boulder, CO, USA ^b Ann and H.J. Smead Aerospace Engineering Sciences, University of Colorado, Boulder, CO, USA

> Received 6 January 2022; accepted 13 September 2022 Available online xxx

Abstract

We investigate the role of mean streamwise pressure gradients in the development of a bluff-body-stabilized premixed flame in the near-wake of the bluff body. To this end, a triangular prism flame holder is situated in three different channel geometries: a nominal case with straight walls, a nozzle with a stronger mean pressure gradient, and a diffuser with a comparatively weaker mean pressure gradient. All geometries are implemented using embedded boundaries, and adaptive mesh refinement is used to locally resolve all relevant thermal (i.e., flame) and fluid-mechanical (i.e., vorticity) scales. A premixed propane flame, modeled using a 66-step skeletal mechanism, interacts with vorticity in the boundary layer of the triangular bluff body in the presence of each mean pressure gradient. Analysis of flame-related enstrophy budget terms reveals key differences in the behavior of baroclinic torque between cases, the specifics of which are tied to larger variations in the mean flow structure, recirculation zone structure, and confinement effects. Our results show that the baroclinic torque changes significantly among the configurations, with the nozzle exhibiting the largest baroclinic torque production. However, these differences are shown to be only a secondary consequence of the background pressure gradient, with the primary consequence being the change in the recirculation zone length resulting from the different channel configurations. These results are relevant for flame stabilization with bluff bodies, where clear understanding of the sensitivities to global mean pressure gradient is important to engineering

© 2022 The Combustion Institute. Published by Elsevier Inc. All rights reserved.

Keywords: Premixed combustion; Turbulent flames; Vorticity dynamics; Bluff body stabilization

E-mail address: peter.hamlington@colorado.edu (P.E. Hamlington).

https://doi.org/10.1016/j.proci.2022.09.064

1. Introduction

Heat release in turbulent premixed flames can either create or destroy vorticity – the square of which is referred to as enstrophy - through a range of complex physical effects. These effects include dilatation, baroclinic torque associated with

1540-7489 © 2022 The Combustion Institute. Published by Elsevier Inc. All rights reserved.

^{*} Corresponding author.

2 S.H.R. Whitman, T.J. Souders, M.A. Meehan et al. | Proceedings of the Combustion Institute xxx (xxxx) xxx

flame-induced density and pressure gradients [1,2], and enhanced viscous dissipation due to increases in gas-phase viscosity from increased temperature [3,4]. The production of enstrophy can, in turn, enhance entrainment and mixing [1], increase the surface area and overall consumption rate of the flame, and ultimately lead to flame disruption and extinction if enstrophy and strain-rate increase sufficiently [5].

The effects of heat release on enstrophy can be examined by analyzing the enstrophy transport equation given by

$$\frac{1}{2} \frac{D\Omega}{Dt} = \omega_i \omega_j S_{ij} + \omega_i \varepsilon_{ijk} \frac{\partial}{\partial x_j} \left(\frac{1}{\rho} \frac{\partial \tau_{kl}}{\partial x_l} \right)
-\Omega S_{kk} + \omega_i \frac{1}{\rho^2} \varepsilon_{ijk} \frac{\partial \rho}{\partial x_j} \frac{\partial p}{\partial x_k},$$
(1)

where $D/Dt = \partial/\partial t + u_i \partial/\partial x_i$, $\Omega = \omega_i \omega_i$ is the enstrophy, $\omega_i = \epsilon_{ijk} \partial u_k / \partial x_j$ is the vorticity, $S_{ij} =$ $(1/2)(\partial u_i/\partial x_j + \partial u_j/\partial x_i)$ is the strain rate tensor, τ_{kl} is the viscous stress tensor, ρ is the density, and p is the pressure. Whereas vortex stretching [the first term on the right-hand side of Eq. (1)] and viscous diffusion [the second term on the right in Eq. (1) are significant in most turbulent flows, including non-reacting flows, dilatation and baroclinic torque [the third and fourth terms, respectively, on the right in Eq. (1) may be strongly enhanced by the presence of a flame [6]. Heat release from reactions leads to local dilatation, and the creation of strong density and pressure gradients by the flame can lead to significant production of vorticity by baroclinic torque [3,7].

Although many prior computational studies have examined enstrophy dynamics in turbulent premixed flames, most such studies have focused on statistically planar or jet configurations, both of which are idealized compared to more realistic geometries. As summarized by Steinberg et al. [3], these studies have shown that the effects of the flame on enstrophy dynamics generally decrease in significance with increasing turbulence intensity. However, recent experiments with bluff-bodystabilized flames [8,9] have shown that the presence of large global mean pressure gradients can cause the baroclinic torque to become a leading-order term in the enstrophy budget, even in highly turbulent conditions. Geikie et al. [9] further showed that the relative strength of baroclinic torque can be controlled by tailoring the mean pressure gradient in the channel holding the bluff-body-stabilized flame. In particular, enstrophy production by baroclinic torque increased substantially when the favorable pressure gradient was increased by adjusting the channel walls from diffuser to nozzle geometries. Similar results have also been obtained by Kazbekov et al. [10,11] for swirl flames.

The bluff-body experiments of Geikie et al. [8,9] indicate several areas for further study, particularly using numerical simulations.

First, indirect and approximate methods were used in the experiments to calculate many of the terms in the enstrophy transport equation – terms that can be directly computed with simulation data, useful to confirm conclusions from the experiments. Second, the optical diagnostics in the bluff-body experiments were, by necessity, limited to the region outside the recirculation zone immediately behind the bluff body. However, substantial flow differences in the near- and far-wake regions raise the possibility that heat release effects on enstrophy vary with distance downstream; full-field simulation data can be used to examine such variations.

In the present study, we specifically examine the effects of mean pressure gradient on dilatation and baroclinic torque by simulating bluff-bodystabilized premixed propane-air flames in nozzle, channel, and diffuser geometries. These simulations are motivated by the experimental configurations studied by Geikie et al. [8,9], although here the computational geometries have been reduced in size (corresponding to lower Reynolds numbers) to attain the very fine resolutions necessary to adequately resolve the flame and compute the highorder gradients required for the enstrophy budget terms in Eq. (1). As such, the present study is focused more on evaluating the conclusions obtained in the experiments than on precisely reproducing the experimental conditions. The simulations are performed using adaptive mesh refinement (AMR) in PeleC [12] to enable high spatial resolution at reasonable computational cost.

2. Numerical simulations

The simulations are performed using the AMReX-based [13] finite-volume code PeleC [12], which solves the fully compressible conservation equations:

$$\frac{\partial \rho}{\partial t} + \frac{\partial \rho u_i}{\partial x_i} = 0, \tag{2}$$

$$\frac{\partial \rho u_i}{\partial t} + \frac{\partial \rho u_i u_j}{\partial x_i} = -\frac{\partial p}{\partial x_i} + \frac{\partial \tau_{ij}}{\partial x_j},\tag{3}$$

$$\frac{\partial \rho E}{\partial t} + \frac{\partial \rho u_i E}{\partial x_i} = -\frac{\partial \rho u_i}{\partial x_i} + \frac{\partial}{\partial x_i} \left(\lambda \frac{\partial T}{\partial x_i} \right) + \sum_k \rho q_k \dot{\omega}_k, \tag{4}$$

$$\frac{\partial \rho Y_k}{\partial t} + \frac{\partial \rho u_i Y_k}{\partial x_i} = -\frac{\partial \mathcal{F}_{k,i}}{\partial x_i} + \rho \dot{\omega_k}.$$
 (5)

Here $E = e + (1/2)u_iu_i$ is the total energy (where e is the internal energy per unit mass), λ

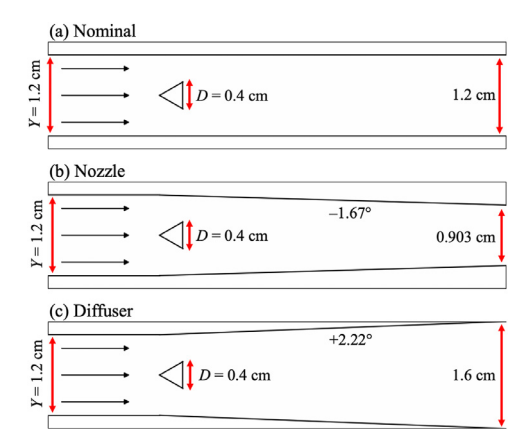


Fig. 1. Two-dimensional cuts of each geometry simulated: (a) A nominal case with flat parallel top and bottom walls, (b) a nozzle with an enhanced favorable pressure gradient, and (c) a diffuser with a less favorable pressure gradient. In all cases the domain length is 6.8 cm.

is the thermal conductivity, Y_k is the mass fraction of the kth chemical species, $\dot{\omega}_k$ is the chemical species reaction source term, and $\mathcal{F}_{k,i}$ is the i-directional species transport flux. The coefficients in the transport fluxes are calculated with polynomial fits and are mixture-averaged to provide temperature-dependent transport properties.

The spatial discretization applies a second-order method-of-lines approach with characteristic extrapolation to cell faces [12]. Operator splitting is used to advance transport equations with explicit source terms. The stiff chemical source terms are advanced implicitly with the GMRES method in the CVODE [14] suite. Transport and chemistry source terms are then used in a global second-order predictor-corrector time-stepping framework. The AMReX framework is used for AMR and provides a regular, box-structured hierarchical series of nested grids on which Eqs. 2–(5) are solved. Each level of mesh refinement increases local grid resolution by a factor of 2. Refinement is grid-based, such that regions of the domain selected for refinement are divided into rectangular "grids" of cells, with grid sizes controlled by specified parameters. These grids also correspond to the parallel decomposition of the domain, with each grid being solved separately on a single processor, with ghost cell data communication as necessary.

2.1. Physical configuration

The three simulation cases illustrated in Fig. 1 consist of: (a) a "nominal" rectangular channel with parallel top and bottom walls (Fig. 1a); (b) a nozzle where the separation between the top and bottom walls decreases in the streamwise direction (Fig. 1b); and (c) a diffuser where the separation between the top and bottom walls increases in the

streamwise direction (Fig. 1c). The wall angles in the nozzle and diffuser cases are -1.67° and 2.22° , respectively, measured with respect to the horizontal.

The bluff body in each case is centered in the channels and has a triangular cross-section with side length D=0.4 cm in all simulations. Because the mesh is box-structured and isotropic, the bluff-body surface is not coincident with cell faces and is implemented with an embedded boundary method [15] within the finite volume framework, with flux corrections accounting for analytic cutcell prescriptions.

A total of four simulations are described here: a three-dimensional (3D) simulation of the nominal case and two-dimensional (2D) simulations of each of the three cases. It will be shown that, for the relatively small geometries examined here, the 3D and 2D results are qualitatively similar, motivating the use of 2D simulations to maintain high spatial resolution while enabling long simulation run-times to obtain adequately converged time-averaged statistics

The overall domain dimensions are 6.8 cm × $Y \times 0.8$ cm for the 3D simulation and 6.8 cm $\times Y$ for the 2D simulations, with the channel height Y = 1.2 cm at the channel inlet. The outlet widens to 1.6 cm at the end of the domain in the diffuser case and shrinks to 0.903 cm in the nozzle case, resulting in inverted inlet to outlet ratios (roughly 4/3 and 3/4, respectively) in the two cases. The different pressure gradients are created by the sloping channel walls, which are also associated with varying degrees of flow confinement. In the 3D simulation, the width in the z-dimension corresponds to two bluff-body diameters, which, according to Refs. [16,17], is sufficient to allow the flow to develop in the spanwise direction at an affordable computational cost. The 2D simulations each have a cell count of roughly 500,000, while the 3D simulation has a cell count of roughly 25 million, although the exact counts vary in time with the adaptive mesh.

At the inflow, Dirichlet boundary conditions are used for the uniform inflow velocity (U_0 = 1, 200 cm/s), the unburnt mixture temperature $(T_u=300 \text{ K})$, the unburnt gas pressure (atmospheric, $p_u = p_{atm}$) and species mass fractions. We enforce a lean equivalence ratio $\phi = 0.65$, where $\phi = (m_{\text{C}_3\text{H}_8}/m_{\text{air}})/(m_{\text{C}_3\text{H}_8}/m_{\text{air}})_{\text{st}}$, with the 'st' subscript denoting stoichiometric conditions. The resulting inflow Reynolds number based on the bluffbody side length is $Re_D = 3$, 102. In the current study, the inflow is uniform without turbulent fluctuations. As such, unsteadiness develops naturally as the result of convective and global instabilities in the bluff-body wake in combination with a very small level of white noise added to the initial conditions. Determining the effects of inflow turbulence is an important area for future study.

4 S.H.R. Whitman, T.J. Souders, M.A. Meehan et al. | Proceedings of the Combustion Institute xxx (xxxx) xxx

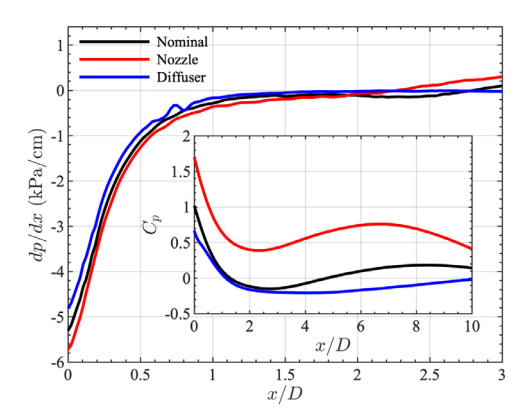


Fig. 2. Time-averaged pressure gradient in the x direction at y = 0.3 cm for the nominal (black lines), nozzle (red lines), and diffuser (blue lines) cases. The inset shows the time-averaged coefficient of pressure, C_p , along the upper wall. (For interpretation of the references to colour in this figure legend, the reader is referred to the web version of this article.)

At the outflow, non-reflecting boundary conditions are applied to velocity and temperature [18] with a fixed atmospheric target pressure. At the top and bottom surfaces, adiabatic (i.e., zero temperature gradient) boundary conditions are used for the temperature and no-slip boundary conditions are used for velocity components. The spanwise direction is periodic for all variables in the 3D case. The 2D models approximate a bluff-body flame with negligible spanwise boundary influences.

For the chemical kinetics model, we use the 25-species, 66-step skeletal propane-air mechanism developed by Zettervall et al. [19], which has been used previously in large eddy simulations of larger bluff-body propane flames [20]. This chemical mechanism has been shown to provide more realistic ignition times and responses to strain when compared to lower-order global mechanisms and other similarly sized skeletal and reduced mechanisms [20]. Simpler mechanisms typically provide poor predictions of ignition time and strain response [21], the latter of which is especially important for these simulations where shear and strainrate effects are strong. The resulting laminar thermal flame width is $\delta_L = 0.66$ mm with unburnt to burnt density and temperature ratios of $\rho_{\rm u}/\rho_{\rm b} =$ 6.45 and $T_{\rm u}/T_{\rm b}=6.43$, respectively.

For the three 2D simulations, Fig. 2 shows mean pressure gradients measured immediately above the bluff body at y = 0.3 cm (where y = 0 cm corresponds to the channel centerline). This figure indicates that the maximum pressure gradient magnitude at this y location is largest in the nozzle and smallest in the diffuser, with the maximum gradient magnitude roughly 15% larger in the nozzle than

the diffuser. At this y location, all cases show a strong favorable pressure gradient close behind the bluff body, transitioning to an adverse axial pressure gradient after $x/D \approx 2.5$ for the nominal and nozzle cases, and after $x/D \approx 5$ for the diffuser. This transition is the approximate center of the recirculation zone in each case. The inset of Fig. 2 further shows the coefficient of pressure $C_p = (p - p_{\rm atm})/(\rho_{\rm u}U_0^2/2)$ measured at the wall as a function of downstream distance x/D.

2.2. Adaptive mesh refinement criteria

For the current study, we locally refine on CO concentration, the vorticity magnitude, and bluff-body walls. The refinement on bluff-body walls is static in time since the bluff body does not move, but the refinement on CO concentration and vorticity tracks structures as they are advected.

The threshold for vorticity magnitude refinement was chosen iteratively relative to the values observed in each case. Given that higher refinement allows for more vorticity generation at the boundary layer of the bluff body and channel walls, the refinement threshold doubles for cells at each AMR level. Because the gradients used in the vorticity calculation are calculated with second-order central differences, this corresponds to the increase in vorticity observed with increasing refinement. The vorticity tagging threshold, ω_{ν} , is thus calculated as $\omega_{\nu} = \omega_0 2^{\ell}$, where ω_0 is a user-specified value (here, $\omega_0 = 1.25 \times 10^4 \text{ s}^{-1}$), and ℓ is the AMR grid level, starting at $\ell = 0$ for the base grid. By tracking vorticity in the AMR procedure, we ensure that the recirculation zone, shear layers, and the near-wake region are well captured, and that strong gradients in velocity, species, temperature, and other flow quantities do not pass across AMR boundaries. The CO concentration is tagged for values above 2.0×10^{-2} g/cm³, relative to the maximum value of 5.0×10^{-2} g/cm³. Because the CO distribution for the flame front is broad relative to other intermediary species, this serves to capture the flame front at high resolution even in areas with weaker vorticity.

The resulting finest mesh resolution in the simulations is $\Delta_{min}=0.04$ mm, giving roughly 16 grid cells per laminar thermal flame width δ_L , thus making the flame well resolved. Additionally, given the relatively low Reynolds number, the turbulence is also highly resolved, making these simulations locally equivalent in scale to direct numerical simulation

3. Results

Fig. 3 shows instantaneous fields of the CH₂O mass fraction, indicative of the flame location, for each of the three 2D simulations. In all cases, immediately behind the bluff body there is essentially no roll-up of the flame. However, as the pres-

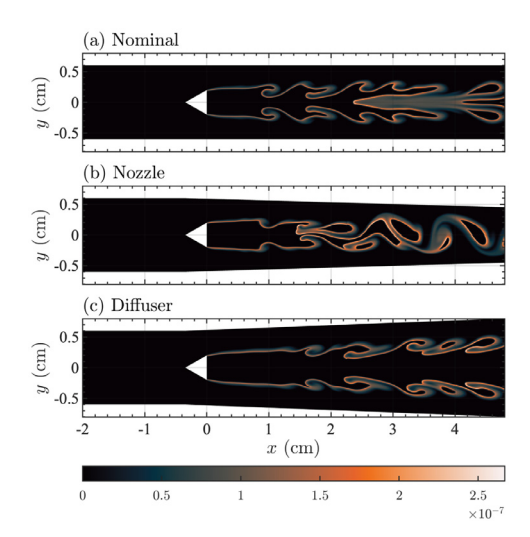


Fig. 3. Instantaneous fields of $\rho Y_{\text{CH}_2\text{O}}$ from the 2D simulations for the nominal (a), nozzle (b), and diffuser (c) cases.

sure gradient magnitude increases from diffuser to nominal to nozzle geometries, perturbation of the flame occurs increasingly close to the bluff body.

The corresponding time-averaged fields of vorticity, dilatation, and baroclinic torque close to the bluff body are shown in Fig. 4, where the region of peak mean heat release rate is shown bounded by green contours. Vorticity is initially generated in the bluff-body boundary layer and advected into the shear layer, where dilatation and baroclinic torque become significant due to the flame. In all cases, the strongest vorticity lies primarily outside the heat release region, and all vorticity at or inside the flame is significantly weaker. This offset is due to the strong streamwise velocity which, combined with the degree of confinement, leads to high strain rates immediately behind the bluff body, keeping the flame confined to the inside of the shear layer. Chaudhuri et al. [5] found this arrangement to be close to blowoff conditions due to the high hydrodynamic strain, which led to localized extinction of a flame stabilized on a disktype bluff body. These localized extinction events allowed for the entrainment of heat into the recirculation zone; the same phenomenon is observed

Towards the center of the recirculation zone, Fig. 4 shows that the nominal and nozzle cases exhibit broadening of the dilatation and baroclinic torque fields. Emerson *et al.* [22] determined that the relative offset of the flame and shear layer was a determining factor in global stability, and that any offset was destabilizing because dilatation would be less effective as a sink for vorticity, leading to stronger shear layer vorticity and a more rapid in-

stability growth rate. Here, despite an offset between the shear layer and heat release, dilatation still serves as a significant sink of enstrophy, as seen in Figs. 4(b,e,h). The location of the flame notwith-standing, thermal expansion and, hence, the dilatational enstrophy sink, continue outside of the maximum heat release zone. Thus, while the degree may be reduced by the offset, dilatation resulting from heat release can have a stabilizing effect even when the shear layer lies outside the flame.

Geikie et al. [8] found that the baroclinic torque near the bluff body must be a source of vorticity rather than a sink, since the pressure gradient was measured to be adverse over the latter part of the recirculation zone. In Fig. 4 we see that this is indeed generally true when the pressure gradient is adverse (i.e., primarily toward the center of the recirculation zone and afterwards). However, in bluffbody flames where the pressure minimum is located downstream from the bluff body, there is a region over which the pressure gradient is favorable. This leads to negative baroclinic torque immediately behind the bluff body in each of the present cases (i.e., it is an enstrophy sink). While dilatation is the strongest enstrophy sink in the shear layer for all cases (despite the offset of the shear layer and the zone of maximum heat release), baroclinic torque acts as a secondary, but still significant, enstrophy sink in this region, as seen in Fig. 4.

Further downstream and inside the heat release region, baroclinic torque transitions to a source. This transition starts shortly upstream of the centerline streamwise pressure minimum (at approximately 0.2 cm for the nominal and nozzle cases and 0.3 cm for the diffuser), but grows stronger closer to the minimum. Downstream of this transition, the contribution is primarily a source within the flame. Outside of the zone of maximum heat release, baroclinic torque does remain an enstrophy sink, even into the region of adverse streamwise pressure gradient, as shown in Figs. 4(c,f,i). This region of split contribution corresponds to the transition from favorable to adverse streamwise pressure gradient. For the diffuser, as compared to the nominal and nozzle cases, the recirculation zone is simultaneously much weaker and much longer, leading to reduced baroclinic torque enstrophy production in the region analyzed.

The broadening of the baroclinic torque enstrophy production region in the nominal and nozzle cases observed in Figs. 4(c,f) is due primarily to stronger vortex roll-up in the shear layers and intermittent pinching events wherein shear layer vortices are pulled towards the center of the recirculation zone, increasing the vorticity in the center of the region and resulting in average pressure minima off the centerline, as can be seen in the overset arrows on Figs. 4(c,f). In 3D simulations and experiments, similar phenomena may be amplified by free-stream turbulence interacting with the shear layer [23].

6 S.H.R. Whitman, T.J. Souders, M.A. Meehan et al. | Proceedings of the Combustion Institute xxx (xxxx) xxx

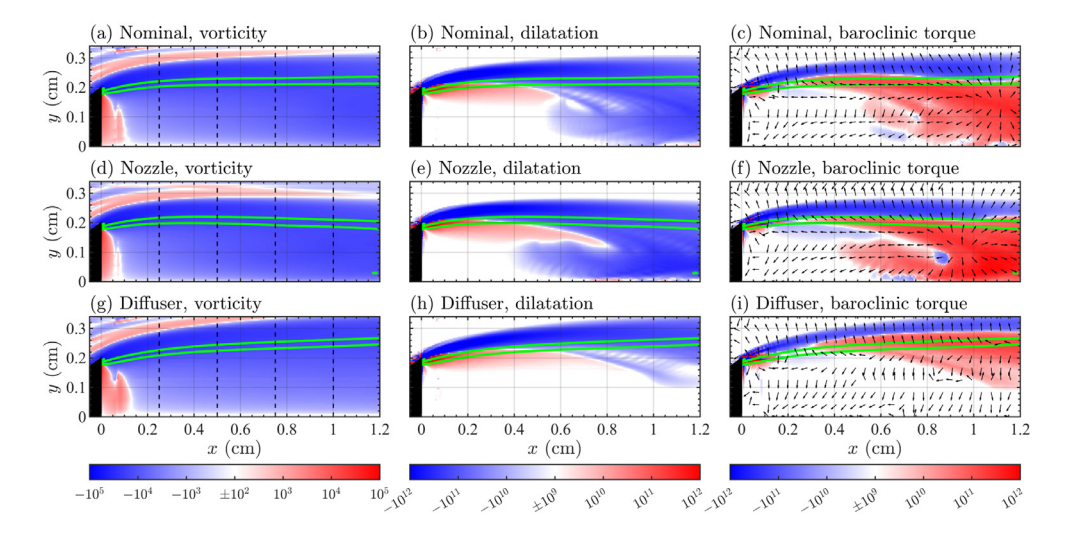


Fig. 4. Time-averaged fields of vorticity magnitude for each of the three cases (panels a, d and g), as well as terms from the enstrophy budget, Eq. (1): enstrophy source from dilatation (panels b, e and h) and from baroclinic torque (panels c, f and i). The region analyzed corresponds to the shear layer immediately behind the bluff body (shown in black). The region of mean peak heat release rate is bounded by green lines for each field. Vertical dashed lines in panels a, d, and g show the locations of the vertical profiles provided in Fig. 5, and arrows on panels c, f and i show the directions of the mean pressure gradient. (For interpretation of the references to colour in this figure legend, the reader is referred to the web version of this article.)

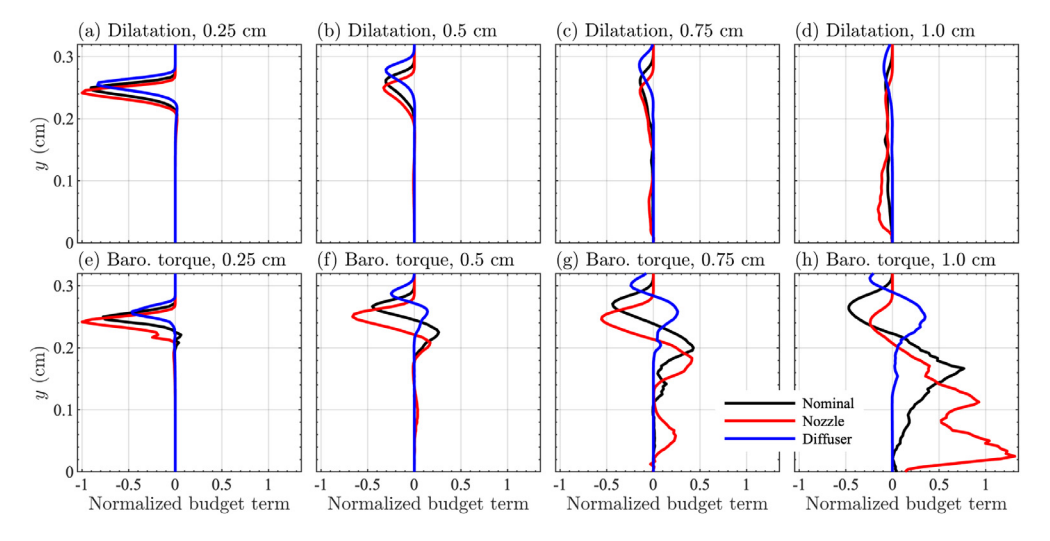


Fig. 5. Time-averaged profiles of dilatation (a-d) and baroclinic torque (e-h) at downstream locations 0.25 cm, 0.5 cm, 0.75 cm, and 1.0 cm (as indicated in Fig. 4) from the 2D simulations of the nominal (black lines), nozzle (red lines), and diffuser (blue lines) cases. Each term is normalized by the maximum budget term value for the nozzle case at 0.25 cm. (For interpretation of the references to colour in this figure legend, the reader is referred to the web version of this article.)

Corresponding profiles of time-averaged dilatation and baroclinic torque at various downstream locations are shown in Fig. 5, allowing a comparison of the relative magnitudes of the budget terms across the three cases. In all cases, dilatation is primarily a sink of enstrophy and decreases in magnitude with downstream location. At each location, the peak magnitude of dilatation is similar across

the three cases, although the peak is closest to the centerline in the nozzle and furthest from the centerline in the diffuser. However, this is primarily a result of the flame and shear layer locations, and there is little effect of background pressure gradient on the strength of the dilatation.

By contrast, the baroclinic torque profiles in the bottom row of Fig. 5 indicate that the baroclinic

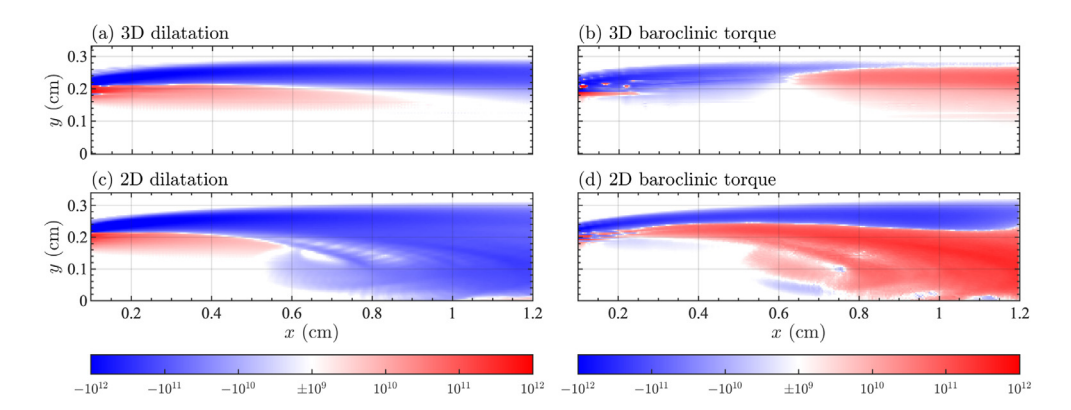


Fig. 6. Fields of time-averaged enstrophy transport contributions from dilatation (panels a and c) and baroclinic torque (panels b and d) for the 3D (a,b) and 2D (c,d) simulations of the nominal case.

torque is a sink near the bluff body that increases in magnitude with increasing favorable pressure gradient (i.e., the nozzle case has the largest magnitude). Downstream, however, as the baroclinic torque becomes a source of enstrophy, the magnitudes become more similar in the nominal and nozzle cases. Yet further downstream, where the baroclinic torque is predominantly positive, the nozzle case again develops larger magnitudes than the nominal case. The baroclinic torque for the diffuser is predominantly small in magnitude throughout, with a transition to weak production of enstrophy far downstream.

These 2D simulation results are, in many respects, qualitatively similar to corresponding results from 3D simulations, as shown in Fig. 6 for the nominal cases. Because the vortex stretching mechanism is absent in 2D simulations, there is no fully developed 3D turbulence and, correspondingly, less mixing downstream than might be expected in a 3D simulation. However, even in the 3D nominal case, the maximum observed value of the vortex stretching term in Eq. (1) is $\sim \mathcal{O}(10^8)$, roughly four orders of magnitude lower than dilatation and baroclinic torque. This is consistent with minimal spanwise instability and breakdown of spanwise vortices near the bluff body and the corresponding similarity between the 2D and 3D simulations there. The low values of vortex stretching are a result of the relatively low values of Re_D , combined with the suppression of shear layer instability by thermal expansion.

Fig. 6 shows that the structure of the dilatation field is similar in both 2D and 3D cases: positive dilatation inside the flame towards the centerline and negative contribution outside the flame, where the shear layer vorticity is strongest (e.g., Fig. 4). There are larger differences between the 2D and 3D cases for the baroclinic torque, although the transition to predominantly positive baroclinic torque downstream of the bluff body is present in both cases.

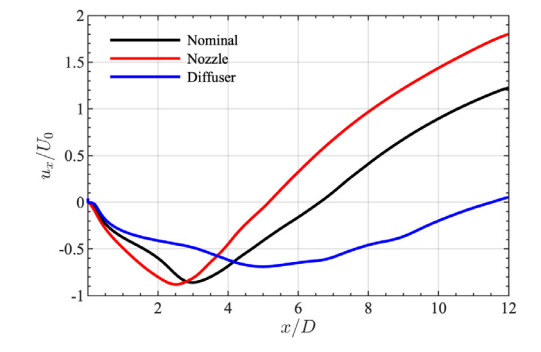


Fig. 7. Streamwise velocity along the centerline through the recirculation zones for the nominal (black line), nozzle (red line), and diffuser (blue line) cases, showing key differences in recirculation zone structure. (For interpretation of the references to colour in this figure legend, the reader is referred to the web version of this article.)

This transition from sink to source is even more pronounced in the 3D case, suggesting that this result is not strictly due to the two-dimensionality of the simulations.

4. Discussion

The results in the previous section motivate further discussion of the impact of channel shape on recirculation zone structure, shown in Fig. 7 for each of the 2D simulation cases. In each case, the tailoring of the channel walls leads to differences in both the recirculation zone size and strength, where strength is measured by the magnitude of negative x-velocity. The recirculation zone length decreases with increasing pressure gradient magnitude, with the diffuser having the longest recirculation zone and the nozzle having the shortest. Both the nozzle and nominal cases have similar recirculation zone strengths, while the diffuser strength is weaker.

Please cite this article as: S.H.R. Whitman, T.J. Souders, M.A. Meehan et al., Pressure gradient tailoring effects on vorticity dynamics in the near-wake of bluff-body premixed flames, Proceedings of the Combustion Institute, https://doi.org/10.1016/j.proci.2022.09.064

7

JID: PROCI [mNS; December 5, 2022;12:59]

S.H.R. Whitman, T.J. Souders, M.A. Meehan et al. | Proceedings of the Combustion Institute xxx (xxxx) xxx

Stronger recirculation zones have lower pressure minima and, therefore, larger mean pressure gradient magnitudes between the center of the recirculation zone and the bulk outer flow. As a result, baroclinic torque contributions are strongest in the nozzle and nominal cases, and weakest in the diffuser case, consistent with the results in Figs. 4 and 5. In addition, baroclinic torque plays a role in determining the flowfield in the downstream region of the recirculation zone, as the positive production from baroclinic torque on the downstream half of the recirculation zone increases shear layer vorticity. This means that in the nominal and nozzle geometries, where the end of the recirculation zone is more abrupt (more so for the nozzle), baroclinic production leads to an increase in the amplitude of shear layer oscillations and in the pinching of the flame. This latter phenomenon is more pronounced in the 2D simulations compared to the 3D nominal case due to the lack of vortex breakdown, explaining the larger baroclinic torque production towards the center of the recirculation zone in the 2D results compared to 3D shown in Fig. 6.

These effects are self-reinforcing; stronger baroclinic torque in the recirculation zone shear layer enhances instability and leads to the aforementioned pinching events, leading to the shorter recirculation zone shown in Fig. 7. For stable flames (i.e., those not experiencing intermittent or sustained local extinction), shorter recirculation zones correspond to stronger pressure gradients and increased misalignment of pressure and density gradients due to the broadening of the shear layers towards the interior flame region as they encompass the recirculation zone. For the diffuser, increasing channel area and, correspondingly, deceleration of the bulk flow lead to expansion of the flame, while lower baroclinic torque production leads to increased flame front stability and a longer recirculation zone.

Ultimately, the tailoring of the global pressure gradient in the present study is directly tied to changes in confinement. Confinement effects are known to impact the development of bluff-body flames. Massey et al. [24] showed that the confinement of bluff-body flames affects the recirculation zone length through a mechanism whereby thermal expansion from the flame increases pressure at the channel walls, increasing the radial pressure gradient. Higher wall pressures were found to be associated with a reduction in recirculation zone length, consistent with the current simulations, as shown in Fig. 7. The present simulations similarly show that the pressure gradient is primarily in the transverse (i.e., y) direction near the flame and shear layer, as indicated by the predominantly vertically oriented unit vectors in Figs. 4(c,f,i). Kim et al. [25] found that, compared to earlier simulations of a confined H₂-air flame anchored on a square prism bluff body [26], a more weakly confined flame saw differences in the flame anchoring location, a wider flame spread in the transverse dimension, and increased transverse "flapping" of the flame. High degrees of confinement have also been shown to be associated with a more dominant sinuous mode in both non-reacting wakes [27] and bluff-body flames [28], an effect likewise observed in the current study: Fig. 3 shows that the nozzle case exhibits a more sinuous wake compared to the symmetric varicose wakes observed for the nominal and diffuser cases. If the flame is so tightly confined that channel boundary layers interact with shear layers from the bluff body, the growth rate of the global sinuous mode is reduced, resulting in stabilization [27,29].

Confinement is therefore relevant for all bluffbody channel flames, although the degree of confinement depends on blockage ratio. Here, we additionally show the degree to which the recirculation zone varies when confinement and global pressure gradients are enforced via channel tailoring. For the nozzle case, production from baroclinic torque leads to a shorter recirculation zone, in a self-reinforcing manner as previously discussed. For the diffuser case, baroclinic torque production is reduced, leading to enhanced flame stability and a longer recirculation zone. In the bluff-body flame experiments of Geikie et al. [9] and Rising et al. [30], channel tailoring was applied starting downstream from the bluff body, so even though the blockage ratio around the bluff bodies of 1/3 was the same as the nominal case considered currently, the recirculation zone appears to be less af-

It may also be possible that a ballistic bluff body such as that employed by Geikie *et al.* [9] would experience less of an impact from channel tailoring on the recirculation zone development, since the flow expansion is forced further upstream to the initial point of the ballistic bluff body, while the blunt trailing edge sees the boundary layers transition into shear layers that are parallel to the channel walls. A more detailed study of the impact of bluff-body geometry on shear layer development in confined bluff-body flames should be undertaken to elucidate these differences.

5. Conclusions

We have performed a series of bluff-body-stabilized flame simulations, varying the channel geometry in which the bluff body is centered, such that the stabilizing prism is in a nozzle in one case, a nominal channel in the second, and a diffuser in the third. This complements the work of Geikie *et al.* [9] and Rising *et al.* [30], who studied stabilized flames for which the bluff body was centered in a nominal channel in all cases, and the tailoring of the walls began approximately one bluffbody length into the recirculation zone. By situating our bluff body in the region of the chan-

JID: PROCI [mNS;December 5, 2022;12:59]

S.H.R. Whitman, T.J. Souders, M.A. Meehan et al. | Proceedings of the Combustion Institute xxx (xxxx) xxx

nel with a mean background pressure gradient, we are able to study the effects of different geometries on the vorticity dynamics in the shear layer development around the recirculation zone, a critical region for flame anchoring, stability and flow development.

Our results show that, although the differences in baroclinic torque magnitude are not large among the three configurations, the nozzle does show the most significant baroclinic torque production, consistent with the findings of Geikie et al. [9]. However, these differences are shown to be a secondary result of the background pressure gradient. The primary cause is the change in the recirculation zone length and geometry that results from the different channel configurations. When the recirculation zone is shorter, as with the nozzle, the pressure minimum lies much closer to the bluff body, and baroclinic torque is a stronger source of vorticity in the downstream half of the recirculation zone. When the recirculation zone is longer, baroclinic torque is a vorticity sink over a much larger region, leading to an overall decrease in vorticity around the recirculation zone. These changes are linked directly to the pressure minimum of the recirculation zone, and we show how the corresponding pressure field dictates the contribution of baroclinicity to enstrophy transport. Between the downstream corners of the bluff body and the center of the recirculation zone, baroclinic torque is an enstrophy sink, whereas over the second half of the recirculation zone (where the mean pressure gradient is adverse) baroclinic torque is an enstrophy

Future work should aim to separate the effects of pressure gradient tailoring from changes in confinement, to the degree possible. Additionally, similar configurations should be studied at larger outer flow scales and higher Reynolds numbers. Perhaps most importantly, the impact of upstream turbulence intensity should be studied, similar to the study by Massey et al. [24] and supplementing the work of Rising et al. [30] with well-resolved 3D simulations. This can be accomplished computationally by either introducing inlet jets prior to the bluff body, or introducing synthetically generated turbulence at the inflow. While turbulence and increased contributions from vortex stretching will likely not change the overall mean behavior of dilatation and baroclinicity immediately behind the bluff body (short of sustained flame disruption or blowoff), the specifics of the unsteady behavior are unknown. An analysis of lifted flames, for example by heating the bluff body, would also allow an examination of the effects of spanwise roller instabilities on flame stabilization. Finally, a detailed study on the impact of bluff-body geometry and wall angle on the impacts of confinement would be useful since the degree to which confinement affects flow development for different geometries is not well understood.

Declaration of Competing Interest

The authors declare that they have no known competing financial interests or personal relationships that could have appeared to influence the work reported in this paper.

Acknowledgments

Helpful discussions with Dr. Kareem Ahmed are gratefully acknowledged. The authors acknowledge support from AFOSR awards FA9550-17-1-0144 and FA9550-18-1-0057, and NSF award 1847111, as well as computing time on the Onyx supercomputer at the Engineer Research and Development Center and the Frontera supercomputer at the Texas Advanced Computing Center.

References

- [1] P. Renard, D. Thevenin, J. Rolon, S. Candel, Prog. Energy Combust. Sci. 26 (3) (2000) 225–282.
- [2] A. Lipatnikov, S. Nishiki, T. Hasegawa, Phys. Fluids 26 (10) (2014) 105104.
- [3] A.M. Steinberg, P.E. Hamlington, X. Zhao, Prog. Energy Combust. Sci. 85 (2021) 100900.
- [4] C. Towery, A. Poludnenko, J. Urzay, J. O'Brien, M. Ihme, P. Hamlington, Phys. Rev. E 93 (5) (2016) 053115.
- [5] S. Chaudhuri, S. Kostka, M. Renfro, B. Cetegen, Combust. Flame 157 (4) (2010) 790.
- [6] R. Darragh, C. Towery, M. Meehan, P. Hamlington, Phys. Fluids 33 (5) (2021) 055120.
- [7] S. Shanbhogue, S. Husain, T. Lieuwen, Prog. Energy Combust. Sci. 35 (1) (2009) 98.
- [8] M. Geikie, Z. Carr, K. Ahmed, D. Forliti, Flow Turbulence Combust. 99 (2) (2017) 487.
- [9] M.K. Geikie, K.A. Ahmed, Combust. Flame 197 (2018) 227–242.
- [10] A. Kazbekov, K. Kumashiro, A. Steinberg, J. Fluid Mech. 876 (2019) 715–732.
- [11] A. Kazbekov, A. Steinberg, Proc. Combust. Inst. 38 (2) (2021) 2949–2956.
- [12] H. Sitaraman, S. Yellapantula, M. de Frahan, B. Perry, J. Rood, R. Grout, M. Day, Combust. Flame 232 (2021) 111531.
- [13] W. Zhang, A. Almgren, V. Beckner, J. Bell, J. Blaschke, C. Chan, M. Day, B. Friesen, K. Gott, D. Graves, et al., J. Open Source Softw. 4 (37) (2019) 1370
- [14] S. Cohen, A. Hindmarsh, P. Dubois, Comput. Phys. 10 (2) (1996) 138.
- [15] R. Pember, J. Bell, P. Colella, W. Curtchfield, M. Welcome, J. Comput. Phys. 120 (2) (1995) 278.
- [16] J. Sykes, T. Gallagher, C.A. Fugger, A. Caswell, B. Rankin, in: AIAA Scitech 2020 Forum, 2020, p. 0436.

Please cite this article as: S.H.R. Whitman, T.J. Souders, M.A. Meehan et al., Pressure gradient tailoring effects on vorticity dynamics in the near-wake of bluff-body premixed flames, Proceedings of the Combustion Institute, https://doi.org/10.1016/j.proci.2022.09.064

9

ARTICLE IN PRESS

JID: PROCI [mNS;December 5, 2022;12:59]

10 S.H.R. Whitman, T.J. Souders, M.A. Meehan et al. | Proceedings of the Combustion Institute xxx (xxxx) xxx

- [17] C. Fureby, 55th AIAA Aerospace Sci. Meeting (2017) 1575.
- [18] J. Blazek, Computational Fluid Dynamics: Principles and Applications, Elsevier (2015), doi:10.1016/ C2013-0-19038-1.
- [19] N. Zettervall, K. Nordin-Bates, E. Nilsson, C. Fureby, Combust. Flame 179 (2017) 1–22.
- [20] C. Fureby, Proc. Combust. Inst. 38 (2) (2021) 3021.
- [21] B. Rochette, F. Collin-Bastiani, L. Gicquel, O. Vermorel, D. Veynante, T. Poinsot, Combust. Flame 191 (2018) 417–430.
- [22] B. Emerson, J. O'Connor, M. Juniper, T. Lieuwen, J. Fluid Mech. 706 (2012) 219–250.
- [23] A. Morales, T. Genova, J. Reyes, I. Boxx, K. Ahmed, Flow Turbulence Combust. 108 (1) (2022) 213.

- [24] J. Massey, I. Langella, N. Swaminathan, J. Fluid Mech. 875 (2019) 699–724.
- [25] Y. Kim, B. Lee, H. Im, Math. Model. Nat. Phenom. 13 (6) (2018) 48.
- [26] B. Lee, C. Yoo, H. Im, Combust. Flame 162 (6) (2015) 2602.
- [27] S. Rees, M. Juniper, J. Fluid Mech. 656 (2010) 309–336.
- [28] B. Emerson, D. Noble, T. Lieuwen, in: 52nd Aerospace Sciences Meeting, 2014, p. 0659.
- [29] O. Tammisola, Linear stability of plane wakes and liquid jets: global and local approach, 2009 Ph.d. thesis, kth.
- [30] C. Rising, A. Morales, M. Geikie, K. Ahmed, Phys. Fluids 33 (1) (2021) 017106.